Coordinatable and High Charge-Carrier-Mobility Water-Soluble Conjugated Copolymers for Effective Aqueous-Processed Polymer–Nanocrystal Hybrid Solar Cells and OFET Applications

*Haotong Wei, Hao Zhang, Gan Jin, Tianyi Na, Guoyan Zhang, Xue Zhang, Yan Wang, Haizhu Sun, Wenjing Tian, and Bai Yang**

A water-soluble conjugated polymer (WCP) poly[(3,4-dibromo-2,5-thienylene vinylene)-*co*-(*p*-phenylene-vinylene)] (PBTPV), containing thiophene rings with high charge-carrier mobility and benzene rings with excellent solubility is designed and prepared through Wessling polymerization. The PBTPV precursor can be easily processed by employing water or alcohols as the solvents, which are clean, environmentally friendly, and non-toxic compared with the highly toxic organic solvents such as chloroform and chlorobenzene. As a novel photoelectric material, PBTPV presents excellent hole-transport properties with a carrier mobility of 5×10^{-4} cm^2 V^{-1} s^{-1} measured in an organic field-effect transistor device. By integrating PBTPV with aqueous CdTe nanocrystals (NCs) to produce the active layer of water-processed hybrid solar cells, the devices exhibit effective power conversion efficiency up to 3.3%. Moreover, the PBTPV can form strong coordination interactions with the CdTe NCs through the S atoms on the thiophene rings, and effective coordination with other nanoparticles can be reasonably expected.

1. Introduction

Water-soluble conjugated polymers (WCPs) play an important role in many areas of modern technology. They are widely used for applications in diagnosis, imaging, and therapy,[1–5] especially in organic light-emitting diodes (OLED) and organic photovoltaics (OPV),[6–11] due to their excellent optical, electrical, and water-soluble properties. WCPs are not only low-cost, flexible, and easily processed, but also clean and environmentally friendly. With respect to their structure, WCPs consist of two parts: one is the conjugated framework in the polymer main-chains, while the other is charged groups in the side-chains, which are responsible for their hydrophilic nature.[9] In recent years, some work has focused on the interfacial modification of OLED[6–8] and OPV[10,11] devices with a thin layer of WCPs to improve electron injection or the interfacial dipole moment due to the locally ordered distribution of charges and the constructed barrier caused by the charged groups. However, the active layer in the photovoltaic devices often consists of two or three materials that are in disorder, and these layers should be thick enough to absorb enough light to generate sufficient charge-carriers. The charges on the side-chains of the WCPs would obstruct the charge-carrier transport, however, and therefore reduce the performance of the devices, which limits the application of WCPs.[12,13] Another choice is to transfer WCPs from a chloroform to a water phase using surfactants, such as sodium dodecylsulphate (SDS), in order to avoid the introduction of the charges on the polymer chains.[14,15] This kind of WCPs disperses in water in the form of microemulsion droplets, which increases the difficulty in controlling the surface morphology.

An effective solution is to remove the charges after forming films, as described in the Wessling polymerization. In our previous work,[16,17] we synthesized poly(*p*-phenylene-vinylene) (PPV) according to the literature,[18] as an excellent photoelectric material, which has been applied in OPV devices as electron donor. However, after decades of investigation, PPV can no longer meet researchers' need in the rapid development of the organic electronics. In our previous study,[19,20] we found that the absorption of the PPV is limited, absorbing light only from about 520 nm, and so most of the visible light is wasted. Moreover, the charge-carrier mobility of PPV is only 1.1×10^{-4} cm^2 V^{-1} s^{-1},[20] and this carrier mobility limits the further improvement of the power conversion efficiency (PCE) of the OPV devices. Exploring a new WCP with a wide absorption range, excellent film-forming properties, ranking stability,

H. Wei, Prof. H. Zhang, T. Na, G. Zhang, X. Zhang, Dr. Y. Wang, Prof. W. Tian, Prof. B. Yang
State Key Laboratory of Supramolecular Structure and Materials
Jilin University
Qianjin Avenue, Changchun, 130012, P. R. China
E-mail: byangchem@jlu.edu.cn
G. Jin, Dr. H. Sun
College of Chemistry
Northeast Normal University
Changchun 130024, P. R. China

DOI: 10.1002/adfm.201300333

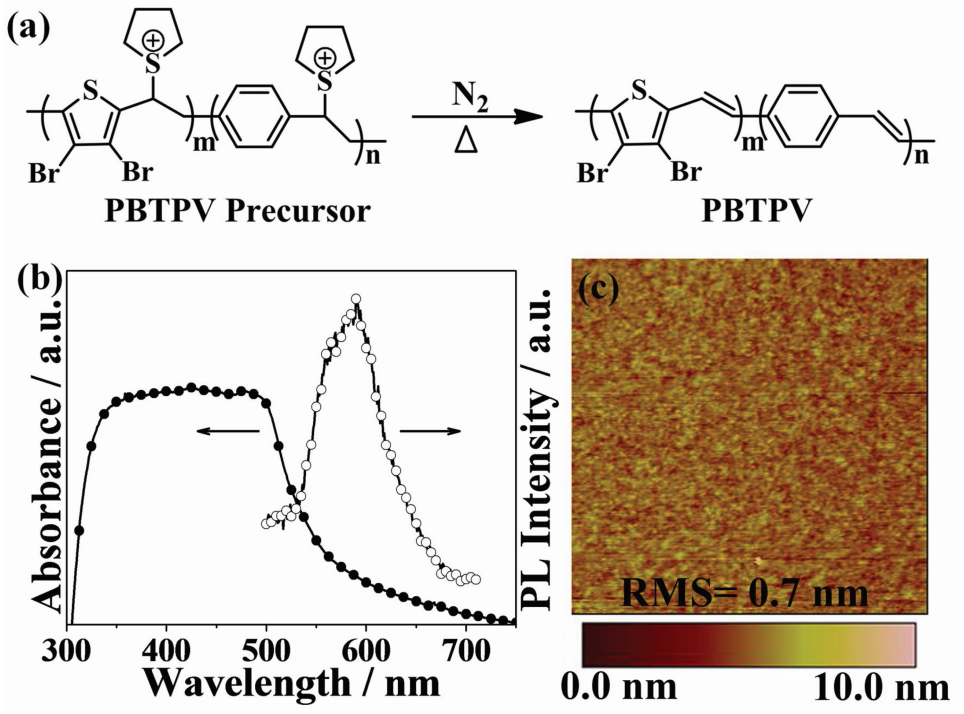

Figure 1. a) The structures of the PBTPV precursor and conjugated PBTPV as well as its formation process. b) The UV–vis absorption and PL emission spectra of the PBTPV. c) AFM (2.5 μm × 2.5 μm) topography of the PBTPV after annealing at 200 °C for 60 min under N_2.

and high charge-carrier mobility is urgently needed. Herein, we report a new WCP synthetic method for poly[(3,4-dibromo-2,5-thienylene vinylene)-*co*-(*p*-phenylene-vinylene)] (PBTPV), containing thienylene units on polymer main chains, through a Wessling polymerization reaction, which is soluble in water/alcohols and exhibits excellent film-forming and hole-transport properties. The organic field-effect transistor (OFET) application proves that the charge-carrier mobility of PBTPV is about 5×10^{-4} cm^2 V^{-1} s^{-1}, which is comparable to common photoelectric polymers. Finally, a water-processed hybrid solar cell consisting of PBTPV and CdTe nanocrystals shows an excellent photovoltaic response and the power conversion efficiency reaches 2.4% (normal type) and 3.3% (inverted type) under AM 1.5G illumination (100 $mW \cdot cm^{-2}$), which is comparable to that of polymer–nanocrystal hybrid solar cells from organic media.

2. Results and Discussion

2.1. Basic Structure and Optical Property of the PBTPV Films

The structure of the PBTPV is described in **Figure 1**a, and the detailed synthetic method of PBTPV can be found in the experimental section. Its structure is demonstrated by nuclear magnetic resonance (NMR) and FT-IR spectroscopies, as shown in Supporting Information Figure S1 and S2, respectively. The PBTPV precursor is easily soluble in water or alcohols because of the positive charged tetrahydrothiophene, and the zeta potential is about 34.8 mV (Supporting Information Figure S4). As a consequence, PBTPV can be easily used by simple solution-processable methods such as spin-coating or ink-jet printing. After annealing under nitrogen, an elimination reaction takes places on the PBTPV precursor chains and the conjugated structure of PBTPV forms, as described in Figure 1a. Meanwhile, the positively charged tetrahydrothiophene units are removed, which assures the efficient transport of electrons and holes. The thermal gravimetric analysis (TGA) results of the PBTPV precursor in Supporting Information Figure S5 illustrates that the tetrahydrothiophene units are removed beginning at a temperature of 150 °C, therefore, the PBTPV precursor is stable under ambient conditions. In addition, PBTPV starts to decompose above 600 °C, and so it can work within a very wide temperature range. As a photovoltaic material, wide absorbance is desired in order to absorb enough light and generate sufficient excitons.[14,21] The UV–vis absorption spectra and fluorescence spectra of the PBTPV are plotted in Figure 1b, and a wide absorption range from 300 to 700 nm is observed, which is red-shifted by about 200 nm relative to the WCP of PPV and the photoluminescence emission is located at about 600 nm. In addition, the PBTPV presents excellent film-forming properties. Calculated by the tapping mode of atomic force microscopy (AFM), the root-mean-square (RMS) roughness of the PBTPV is only 0.7 nm relying on a simple spin-coating method, and the whole film is almost the same within a square area of 2 cm × 2 cm.

2.2. OFET Application Based on Aqueous PBTPV Material

OFETs are particularly attractive candidates for a broad range of low-cost, flexible electronic applications, including electronic

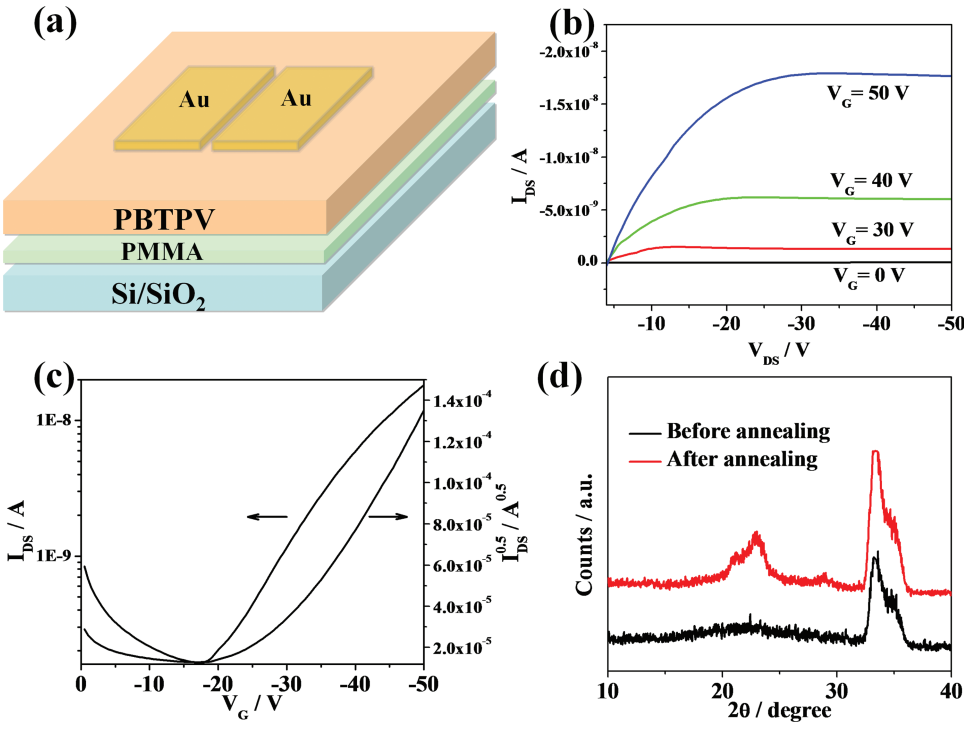

Figure 2. a) The structural scheme of the OFET comprising a PBTPV thin film, 300 nm thick SiO_2 insulator layer modified with PMMA, a heavily doped ni-type Si wafer as the gate electrode, and Au as the source and drain electrodes. b) Output characteristic of an OFET in the *p*-channel mode (from bottom to top, the V_G increased from 0 to 50 V); drain current versus V_{DS} is plotted. c) Drain current I_{DS} versus V_G characteristics of the OFET in the saturation regime at a drain-source voltage V_{DS} of 50 V. d) XRD characterization of the PBTPV before and after annealing under N_2.

paper and chemo-/biosensors.[22,23] Many polymers have been employed for OFET applications,[24–26] but no effective WCPs have been found to demonstrate the OFET property. In order to measure the charge-carrier mobility of the PBTPV, we prepared a simple bottom gate, top contact (BG-TC) field-effect transistor. **Figure 2**a shows the basic OFET structure: 110 nm thickness poly(methyl methacrylate) was spin-coated on a 300 nm thermally oxidized SiO_2 layer as the gate dielectric with heavily doped silicon wafers as the back gate electrode. The current I_{DS} modulated by V_G is approximately determined from the following equation:[27–30]

$$I_{DS} = (W)2L)C_i\mu(V_G - V_T)^2 \qquad \text{(saturation regime)} \qquad (1)$$

Where μ is the field-effect mobility, I_{DS} is the drain current between the drain and source electrodes, L and W are the channel length and width, respectively, C_i is the insulator capacitance per unit area, V_G is the applied gate voltage, and V_T is the extrapolated threshold voltage. In the saturation regime, we use this equation to estimate the charge-carrier mobility μ. From the slope of the plot of $I_D^{0.5}$ versus V_G, μ can be calculated. From Figure 2b we see that PBTPV has good hole-transport ability, and an obvious saturation current is observed at high V_{DS}. The relationship between V_G and I_{DS} is plotted in Figure 2c. The charge-carrier mobility is calculated to be about 5×10^{-4} cm^2 V^{-1} s^{-1}, and the on/off ratio is more than 10^3 when V_G is 50 V. We attribute the high charge-carrier mobility to the high electron density of the thiophene unit, the conjugated structure, and the improved crystallization behavior after annealing. X-ray diffraction (XRD) is employed to study the crystallization process of the PBTPV film before and after annealing. Figure 2d shows that the peak located at 34° enhances after annealing, which indicates that the crystallization is improved. In addition, a new peak appears at 23°, demonstrating a new crystal surface is created due to the formation of a conjugated structure. This novel conjugated structure introduces intermolecular π–π interaction and forms a regularly packed structure as well as a novel crystalline surface.[17]

Figure 3a,b present the optimized electron delocalization MO diagram of the polymer repeating units. Complete delocalization of the electrons can be observed in both of the highest occupied molecular orbital (HOMO) and lowest unoccupied molecular orbital (LUMO) levels. This repeating unit represents the polymer chain in which it is possible to transport both type of charges (electrons and holes). The results from the theoretical calculations with respect to the HOMO level is about –5.28 eV, which is consistent with the value obtained from ultraviolet photoelectron spectroscopy (UPS) measurements (–5.2 eV) shown in Figure 3c,d. The –5.2 eV energy alignment favors hole transport and matches well with the photovoltaic materials commonly used such as poly(ethylenedioxythiophene):poly(styrenesulfonate) (PEDOT: PSS) and Au. For these reasons, we believe that the PBTPV can be applied in solar cell applications.

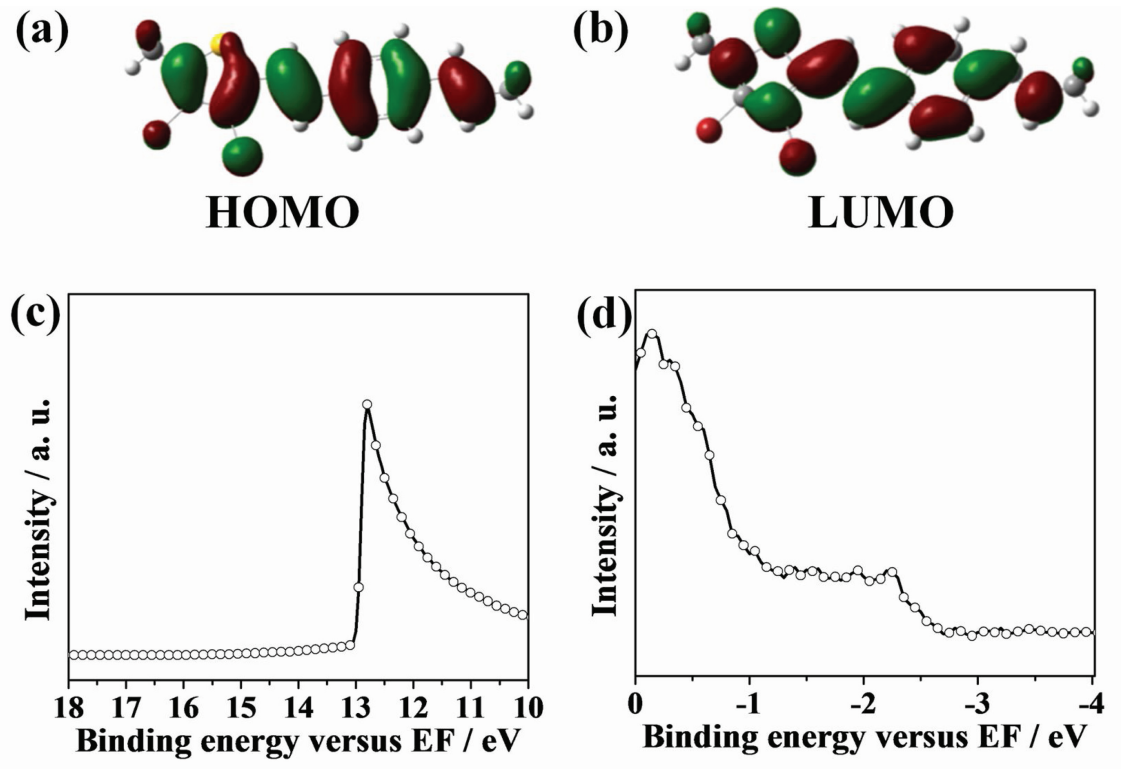

Figure 3. Optimized electron delocalization MO diagram of the PBTPV repeating units: a) HOMO energy level and b) LUMO energy level. c,d) UPS spectrum of the PBTPV: c), cutoff and d) Fermi-edge regions; the *x*-axis shows the binding energy relative to the Fermi level of each material and the HOMO energy is calculated to be −5.2 eV.

2.3. Aqueous-Processed Hybrid Solar Cells Employing PBTPV and CdTe Nanocrystals

Considering the water-soluble properties as well as the concept of green chemistry,[14,31–35] we prepared aqueous-processed hybrid solar cells comprised of PBTPV as the donor and CdTe NCs as the acceptor in order to combine both the low-cost and flexible properties of the polymer with the high charge-carrier mobility of the NCs.[31,34–44] Relying on the HOMO level and the bandgap calculated from the absorption spectra, the energy band structure of the PBTPV is easily described, and is well-matched with the CdTe NCs. Based on the different energy structures of interface-modified materials, we designed both normal structure and inverted structure devices, as shown in **Figure 4**a,b. The normal structure device uses ITO/PEDOT:PSS/PBTPV:CdTe NCs/TiO_x/Al and the inverted structure is built as ITO/TiO_2/PBTPV:CdTe NCs/MoO_3/Au, wherein PEDOT:PSS and MoO_3 are used as hole-transport layers, while TiO_x and TiO_2 are employed as electron-transport layers.[35,45,46] The charge-carriers are transported in opposite directions. The surface morphology of the active layer is studied with AFM, and the corresponding height images of the active layer shown in Figure 4c,d indicate the obvious phase separation on the nanoscale, as well as that an efficient interpenetrating network is established. While the surface of the inverted device is more homogeneous than the normal one, the surface roughness is only 3.0 nm lower than the active layer on PEDOT:PSS, which may be attributed to the partial dissolution of PEDOT:PSS by the aqueous active layer resulting in some bad points or cracks. We observe the growth of the CdTe NCs from about 2 to about 14 nm after annealing under N_2 (Supporting Information Figure S6). These annealed NCs connect with each other and promote the formation of an interpenetrating network as well as electron-transport paths.[34] Meanwhile, the non-conductive ligands on the CdTe NC surfaces are removed during the annealing process. 2-Mercaptoethylamine, the surface ligands on the NCs, contained a characteristic N element, and we detected the obvious decrease of the surface ligands content as the N1s peak disappeared after annealing. Calculated from the XPS data in **Figure 5**a, the surface ligand content decreases to only 9.7% of the original after annealing. Therefore, the conductivity of the NCs might be improved, benefiting from both the effective interpenetrating network and reduced content of surface ligands. In order to characterize the electron mobility of the NCs, electron-only carrier mobility was measured according to a similar method with a diode configuration of ITO/Al/PBTPV:CdTe NCs/LiF/Al using the space-charge-limited-current (SCLC) model at low voltage[20] which is described by:

$$J = 9\varepsilon_0\varepsilon_r\mu V^2/8L^3 \quad (2)$$

Where ε_0 is the permittivity of free space (8.85×10^{-12} F m^{-1}), ε_r is the dielectric constant of the CdTe NCs (assumed to 3), μ is the mobility of an electron, V is the applied voltage, and L

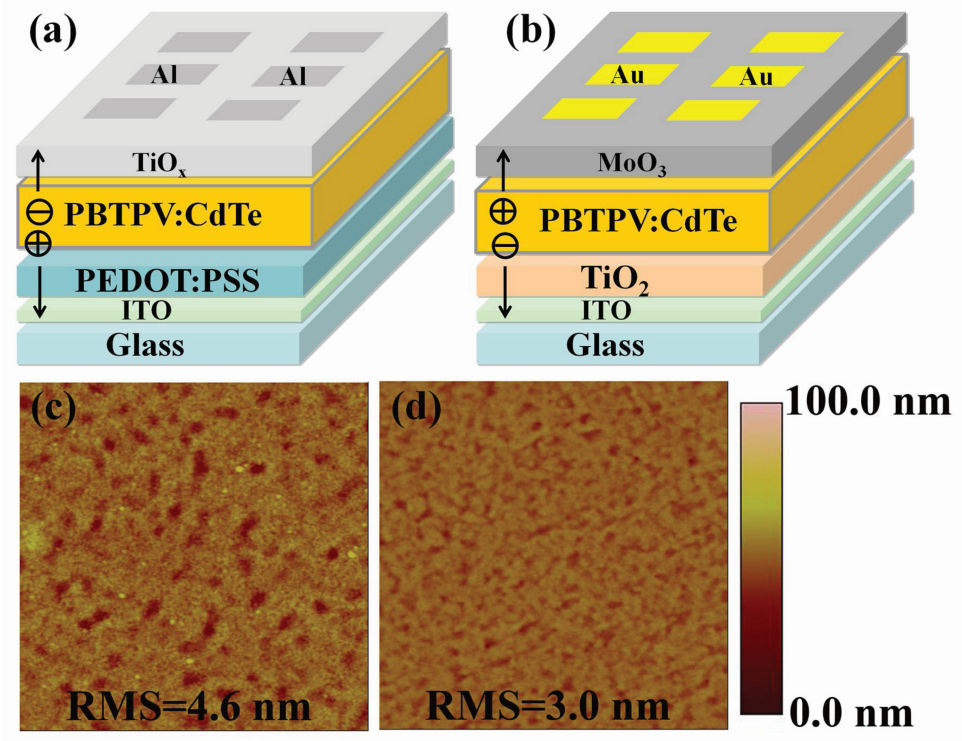

Figure 4. Different device structures result in different charge-carrier transport directions: in the normal structure device (a) PEDOT:PSS is used to collect holes and TiO_x is employed to transport electrons; in the inverted structure device (b) MoO_3 exists as the hole transport layer while TiO_2 is the electron transport layer. c,d) The corresponding AFM (5 µm × 5 µm) topography images; the RMS roughness of the normal structure device (4.6 nm) is larger than the inverted one (3.0 nm), which may be caused by dissolution of the PEDOT:PSS by the aqueous active layer to some extent.

is the film thickness. By fitting the results to a space-charge-limited form, $J^{0.5}$ versus V_{appl} is plotted in the Figure 5b. The thickness of the blend film was about 100 nm, which was determined by the Ambios Tech. XP-2 profilometer. The electron mobility of the CdTe NCs is about 2.03×10^{-4} cm^2 V^{-1} s^{-1}, which is similar to the hole mobility of the PBTPV. Effective charge-carrier transport is based on balanced electron/hole mobility, which indicates a possible photovoltaic response. The energy structures of the devices are presented in **Figure 6**a,b.

We selected a proper interfacial modification layer to introduce either electrons or holes and to promote exciton separation. In the normal devices, amorphous TiO_x is employed as the electron extraction layer, meanwhile the network structure effectively protects the active layer from exposure to water and oxygen. TiO_2 in the inverted structure was processed at 350 °C to form the anatase phase. The crystallization of TiO_2 increases the conductivity and electron transport ability, and the energy structure of crystalline TiO_2 is well-matched with the CdTe NCs

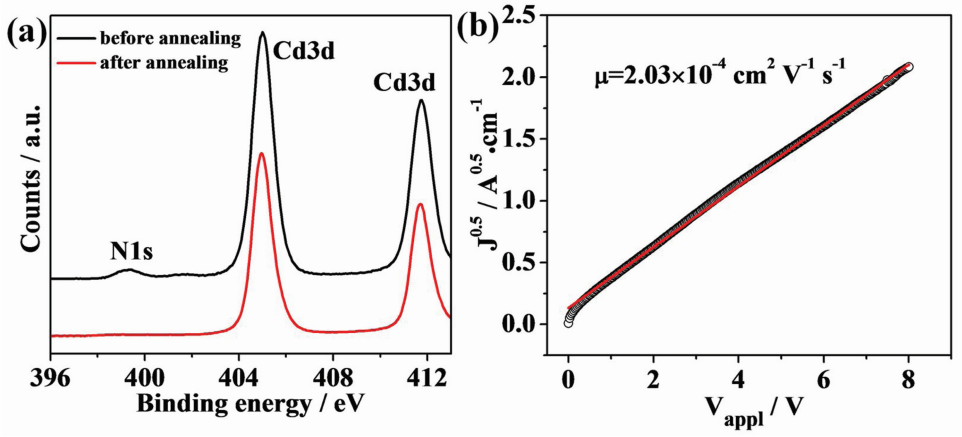

Figure 5. a) XPS spectra of Cd3d and N1s in the CdTe NCs films before and after annealing. b) Results for the electron-only carrier mobility device making use of the PBTPV:CdTe NC hybrid film. The electron mobility of the CdTe NCs reaches 2.03×10^{-4} cm^2 V^{-1} s^{-1}.

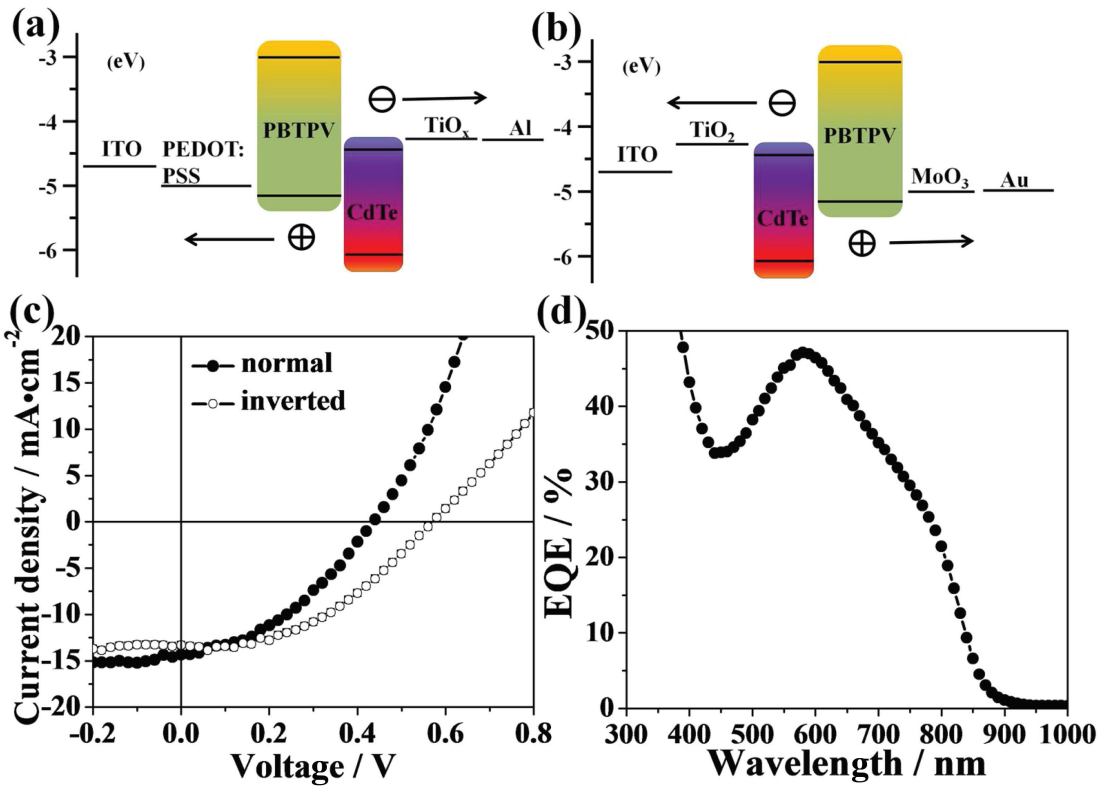

Figure 6. Energy structure schemes of the a) normal and b) inverted structure devices. The staggered energy level arrangements ensure effective charge-carrier transport. c) The corresponding device performance of the normal and inverted structure devices, respectively. d) EQE measurement of the normal device.

Table 1. Current – voltage characteristics of the photovoltaic devices with different device types.

Device type[a)]	J_{sc} [mA cm^{-2}]	V_{oc} [V]	FF [%]	PCE [%]
Normal	14.4	0.44	38.3	2.43
Inverted	13.3	0.58	43.2	3.33

[a)]The device types (including normal and inverted devices) are each modified with the corresponding interfacial layer.

for the prevention of holes and transport of electrons. The corresponding photovoltaic performance is shown in Figure 6c, and the normal type device gives a J_{sc} of 14.4 mA cm^{-2}, V_{oc} of 0.44 V, FF of 38.3%, and PCE of 2.43%, while the inverted type device presents a J_{sc} of 13.3 mA cm^{-2}, V_{oc} of 0.58 V, FF of 43.2%, and PCE of 3.33% (summarized in **Table 1**). The V_{oc} of the inverted device is higher than those of the normal devices, because the leakage current may be more serious in the normal devices, which results in a low V_{oc} as well as a low FF, even though the PEDOT:PSS has been already baked at a high temperature. The photovoltaic response benefits from the interpenetrating network structure of the two phases that results from the CdTe NCs grows during the annealing process. The external quantum efficiency (EQE) of the device is plotted in the Figure 6d, the device is sensitive to a wide spectrum response ranging from 300 to 900 nm, because larger NCs have an absorption red-shift compared to that of smaller NCs.

The S atoms on the thiophene rings of PBTPV can provide effective coordination to the CdTe NCs, and we observe a shift in the peaks of the FT-IR spectrum (**Figure 7**) for the PBTPV

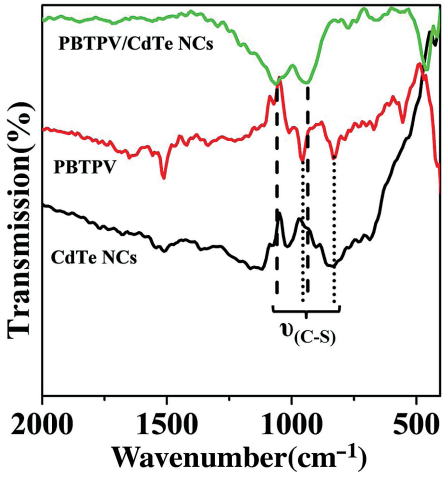

Figure 7. FT-IR spectrum of the CdTe NCs, PBTPV, and PBTPV:CdTe NC hybrid films after annealing. The shift of the stretching vibration peak of the PBTPV after hybridization with CdTe NCs is attributed to the strong coordination between PBTPV and CdTe NCs.

resulting from the C–S bond stretching vibration due to its hybridization with the CdTe NCs. The peaks located at 956 and 830 cm^{-1} shift to 1064 and 943 cm^{-1}, respectively, due to the strong coordination interactions. Meanwhile, most IR peaks of the CdTe NCs disappear, which may be a result from the coordination bond, which reconstruct the surface properties of the CdTe NCs making the interaction between the small molecules and CdTe NCs weaker. We believe that the excellent photovoltaic response is partly due to the strong coordination interactions that led to the charge transfer from PBTPV to the CdTe NCs. The optimized theoretical calculations for the electron delocalization in the LUMO diagrammed in Figure 3b indicates that the S atoms are rich in electron density in the LUMO energy level, so the excited electrons will be transferred most effectively from PBTPV to CdTe NCs through the S atoms. Due to the strong coordination interaction with the S atoms, many nanoparticles are prepared from the small molecular ligands containing –SH. Therefore, PBTPV is also expected to form strong interaction with many other nanoparticles.

3. Conclusions

A new type WCP of PBTPV is synthesized for the first time making use of molecular design. The excellent film-forming properties, stability, and photoelectric response guarantee suitability for OFET and aqueous-processable hybrid solar cell applications. The carrier mobility of the aqueous PBTPV is about 5×10^{-4} cm^2 V^{-1} s^{-1} and the PCE of the aqueous-processed PBTPV/CdTe NCs hybrid photovoltaic device reaches 3.3%, which is within the same level as that of the oil-processed hybrid photovoltaic devices. The excellent photovoltaic response is based on the coordination interaction between PBTPV and the CdTe NCs, which results in effective charge transfer from PBTPV to the CdTe NCs. High performance devices or other applications using PBTPV can reasonably be expected.

4. Experimental Section

Materials: Tellurium powder (200 mesh, 99.8%), *R*,R_0-dichloro-*p*-xylene (98%), and tetrahydrothiophene (99%) were all purchased from Aldrich Chemical Corp. 2-Mercaptoethylamine (MA, 98%) was obtained from Acros. PEDOT:PSS (Clevios PVP. Al 4083) was provided by H. C. Starck Inc. Sodium borohydride ($NaBH_4$, 99%) and $CdCl_2$ (99+%) was commercially procured. All of the solvents were analytical grade and used as received.

Preparation of PBTPV Precursor: The synthetic method for PBTPV is based on two similar reactions: chloromethylation[47] and Wessling polymerization.[16–18] The synthesis is described as follows: a stream of dry hydrogen chloride was added to a stirred solution of 1.25 g paraformaldehyde, 0.5 g $ZnCl_2$, and 2.5 mL of concentrated HCl, allowing the temperature to rise to 50–60 °C, until the solution was saturated. At this point 3 mL of 3,4-dibromothiophene was added dropwise with stirring. After the mixture had been stirred for 6 h, the oily lower layer was siphoned off and washed with cold water several times. The oil was filtered to remove some paraformaldehyde, and then 30 mL methanol was added, followed by the 2.6 mL tetrahydrothiophene. This solution was kept at 50 °C for 24 h to convert the 2,5-dichloro-methyl-3,4-dibromo-thiophene to the sulfonium salt monomer (M_1). The *p*-xylylenebis (tetrahydrothiophenium chloride) (M_2) was prepared using the reaction between *p*-xylylene dichloride and tetrahydrothiophene at 50 °C for 24 h in a 1:2 molar ratio. PBTPV was polymerized by adding 10 mL 0.4 M NaOH to 10 mL of a mixture of 1.24 g M_1 and 0.56 g M_2 in methanol. This solution was cooled to 0–5 °C in an ice bath under nitrogen. The reaction proceeded for 1 h and then was terminated by addition of 0.4 M HCl aqueous solution to neutralize the solution. The aqueous solution of the PBTPV precursor was dialyzed against deionized water for one week.

Preparation of MA-Capped CdTe NCs: Typically, aqueous precursors of CdTe NCs were obtained by injecting a freshly prepared solution of NaHTe into 12.5 mM N_2-saturated $CdCl_2$ solutions in the presence of MA at a pH range of 5.5–6.0. The molar ratio of Cd^{2+}/MA/HTe^- was set as 1:2.4:0.2. The resultant precursor solutions were refluxed at 100 °C to maintain the growth of NCs; their sizes increased with the reflux duration. After preparation, the NC solution was centrifuged at a speed of 8000 rpm with the addition of isopropanol to remove superfluous salts and MA. Then the precipitated NCs were redissolved in deionized water at a concentration of about 70 mg mL^{-1}.

OFET Preparation: OFETs were fabricated in a top-contact configuration on heavily doped n-type Si wafers covered with 300 nm thick thermally grown SiO_2. The Si/SiO_2 substrates were carefully cleaned and handled with UV–O_3 radiation for at least 20 min. 110 nm PMMA was spin-coated on the substrates followed by the aqueous polymer using a 5.0 mg mL^{-1} water solution at 1000 rpm for 120 s, and was subsequently dried at 200 °C for 1 h in a glove box. Au drain and source electrodes (thickness 60 nm) were deposited in vacuum through a shadow mask. The channel length (*L*) and width (*W*) were 50 μm and 1000 μm, respectively. OFET characteristics were measured inside a glove box by using a semiconductor device analyzer, Agilent Technologies B1500A.

Preparation of the Aqueous-Processed Hybrid Devices: i) For the normal structure device, ITO-coated glass substrates were first treated with ultrasonic consequently in chloroform, acetone, and isopropanol. Next, the substrates were rinsed with deionized water before drying in an N_2 flow, followed by oxygen plasma treatment for 5 min; then spin-coating of the PEDOT:PSS layer (45 nm) at 3000 rpm for 60 s, and annealing at 250 °C for 30 min under N_2 in order to avoid dissolution by the active layer. The photoactive layer was formed by spin-coating (at 600 rpm) with an aqueous solution containing the PBTPV precursor and CdTe NCs with a weight ratio of 1:28. The blend film (about 100 nm) was annealed at 300 °C for 60 min in the glove box, and a thin layer (about 10 nm) of TiO_x was spin-coated on the active layer and heated for only 10 min, followed by evaporation of Al electrode with a 5 mm^2 mask. ii) For the inverted structure device, after the plasma treatment for 5 min, ITO-coated glasses were spin-coated with TiO_2 and heated at 350 °C for 15 min. After spin-coating the active layer at 700 rpm, the blend film (about 75 nm) was annealed at 300 °C for 60 min in the glove box, followed by evaporation of MoO_3 (5 nm) and Au electrode (60 nm) with a 5 mm^2 mask.

Characterization: UV–vis spectra were acquired on a Shimadzu 3600 UV–vis–NIR spectrophotometer. Fluorescence spectra were acquired on a Shimadzu RF-5301 PC spectrofluorimeter and the excitation wavelength was 365 nm. AFM images were recorded in tapping mode with a Digital Instruments NanoScope IIIa under ambient conditions. XRD investigations were carried out by using Siemens D5005 diffractometer. TEM images were recorded on a JEOL-2010 electron microscope operating at 200 kV. The film thicknesses were measured on an Ambios Tech. XP-2 profilometer. EQE was measured under illumination of monochromatic light from the xenon lamp using a monochromator (Jobin Yvon, TRIAX 320) and detected by a computer-controlled Stanford SR830 lock-in amplifier with a Stanford SR540 chopper. The energy band values were measured in an integrated ultrahigh vacuum system equipped with multitechnique surface analysis system (VG ESCALAB MK II spectrometer) UPS. UPS was measured with the He (I) (21.2 eV) line using a negative bias voltage applied to the samples in order to shift the spectra from the spectrometer threshold. XPS was investigated by using ESCALAB 250 spectrometer with a mono X-ray source Al Ka excitation (1486.6 eV). The ^1H NMR spectra were recorded using a Bruker AVANCEIII500 spectrometer at

500 MHz. Matrix-assisted laser desorption/ionization reflect time-of-flight (MALDI-TOF) MS was recorded on Bruker autoflex speed TOF with DCTB as the matrix. Zeta potential measurements were performed using a Zetasizer Nano-ZS (Malvern Instruments) and the result was measured for more than 5 times and the average value is given. The current density–voltage (*J–V*) characterizations of PV devices under white-light illumination from an Sciencetech 500-W solar simulator (AM 1.5G, 100 mW cm^{-2}) were measured on computer-controlled Keithley 2400 Source Meter measurement system in a glove box filled with nitrogen atmosphere (<1 ppm H_2O and <1 ppm O_2). All the other measurements were performed under ambient atmosphere at room temperature.

Supporting Information

Supporting Information is available from the Wiley Online Library or from the author.

Acknowledgements

This project was supported by the NSFC (21221063 and 91123031) and the National Basic Research Development Program of China (2012CB933802). The authors acknowledge the Open Project of State Key Laboratory of Polymer Materials Engineering China (KF200906). Figure 2 was corrected on August 26, 2013

Received: January 28, 2013
Published online: March 15, 2013

[1] X. L. Feng, L. B. Liu, S. Wang, D. B. Zhu, *Chem. Soc. Rev.* **2010**, *39*, 2411.
[2] C. L. Zhu, L. B. Liu, Q. Yang, F. T. Lv, S. Wang, *Chem. Rev.* **2012**, *112*, 4687.
[3] B. Liu, S. Wang, G. C. Bazan, A. Mikhailovsky, *J. Am. Chem. Soc.* **2003**, *125*, 13306.
[4] B. Liu, G. C. Bazan, *Chem. Mater.* **2004**, *16*, 4467.
[5] B. S. Gaylord, A. J. Heeger, G. C. Bazan, *J. Am. Chem. Soc.* **2003**, *125*, 896.
[6] H. B. Wu, F. Huang, Y. Q. Mo, W. Yang, D. L. Wang, J. B. Peng, Y. Cao, *Adv. Mater.* **2004**, *16*, 1826.
[7] B. Liu, W. L. Yu, Y. H. Lai, W. Huang, *Chem. Commun.* **2000**, 551.
[8] W. L. Ma, P. K. Iyer, X. Gong, B. Liu, D. Moses, G. C. Bazan, A. J. Heeger, *Adv. Mater.* **2005**, *17*, 274.
[9] F. Huang, H. B. Wu, Y. Cao, *Chem. Soc. Rev.* **2010**, *39*, 2500.
[10] Z. C. He, C. M. Zhong, X. Huang, W. Wong, H. B. Wu, L. W. Chen, S. J. Su, Y. Cao, *Adv. Mater.* **2011**, *23*, 4636.
[11] Z. C. He, C. Zhang, X. F. Xu, L. J. Zhang, L. Huang, J. W. Chen, H. B. Wu, Y. Cao, *Adv. Mater.* **2011**, *23*, 3086.
[12] J. H. Yang, A. Garcia, T. Q. Nguyen, *Appl. Phys. Lett.* **2007**, *90*, 103514.
[13] I. Haeldermans, I. Truijen, K. Vandewal, W. Moons, M. K. Van Bael, J. D'Haen, J. V. Manca, J. Mullens, *Thin Solid Films* **2008**, *516*, 7245.
[14] T. R. Andersen, T. T. Larsen-Olsen, B. Andreasen, A. P. L. Böttiger, J. E. Carlé, M. Helgesen, E. Bundgaard, K. Norman, J. W. Andreasen, M. Jørgensen, F. C. Krebs, *ACS Nano* **2011**, *5*, 4188.
[15] Y. Nan, X. Hu, T. T. Larsen-Olsen, B. Andreasen, T. Tromholt, J. W. Andreasen, D. M. Tanenbaum, H. Z. Chen, F. C. Krebs, *Nanotechnology* **2011**, *22*, 475301.
[16] H. Z. Sun, H. Zhang, J. H. Zhang, H. T. Wei, J. Ju, M. J. Li, B. Yang, *J. Mater. Chem.* **2009**, *19*, 6740.
[17] H. T. Wei, H. Z. Sun, H. Zhang, C. Gao, B. Yang, *Nano Res.* **2010**, *3*, 496.
[18] J. H. Burroughes, D. D. C. Bradley, A. R. Brown, R. N. Marks, K. Mackay, R. H. Friend, P. L. Burns, A. B. Holmes, *Nature* **1990**, *347*, 539.
[19] H. T. Wei, H. Z. Sun, H. Zhang, W. L. Yu, F. Zhai, Z. X. Fan, W. J. Tian, B. Yang, *J. Mater. Chem.* **2012**, *22*, 9161.
[20] H. T. Wei, H. Zhang, H. Z. Sun, W. L. Yu, Y. Liu, Z. L. Chen, L. Y. Cui, W. J. Tian, B. Yang, *J. Mater. Chem.* **2012**, *22*, 17827.
[21] Z. C. He, C. M. Zhong, S. J. Su, M. Xu, H. B. Wu, Y. Cao, *Nat. Photonics* **2012**, *6*, 591.
[22] A. N. Sokolov, B. C. Tee, C. J. Bettinger, J. B. Tok, Z. Bao, *Acc. Chem. Res.* **2012**, *45*, 361.
[23] C. Di, F. J. Zhang, D. B. Zhu, *Adv. Mater.* **2013**, *25*, 313.
[24] B. Souharce, C. J. Kudla, M. Forster, J. Steiger, R. Anselmann, H. Thiem, U. Scherf, *Macromol. Rapid Commun.* **2009**, *30*, 1258.
[25] Y. G. Chen, C. F. Liu, H. K. Tian, C. Bao, X. J. Zhang, D. H. Yan, Y. H. Geng, F. S. Wang, *Macromol. Rapid Commun.* **2012**, *33*, 1759.
[26] K. L. Cao, X. N. Sun, Q. Zhang, Y. Q. Liu, *Macromol. Chem. Phys.* **2012**, *213*, 917.
[27] J. Zaumseil, H. Sirringhaus, *Chem. Rev.* **2007**, *107*, 1296.
[28] C. Kanimozhi, N. Yaacobi-Gross, K. W. Chou, A. Amassian, T. D. Anthopoulos, S. Patil, *J. Am. Chem. Soc.* **2012**, *134*, 16532.
[29] K. Baeg, D. Khim, J. Kim, B. Yang, M. J. Kang, S. Jung, I. You, D. Kim, Y. Noh, *Adv. Funct. Mater.* **2012**, *22*, 2915.
[30] J. G. Labram, E. B. Domingo, N. Stingelin, D. D. C. Bradley, T. D. Anthopoulos, *Adv. Funct. Mater.* **2011**, *21*, 356.
[31] H. T. Wei, H. Zhang, H. Z. Sun, B. Yang, *Nano Today* **2012**, *7*, 316.
[32] R. Søndergaard, M. Helgesen, M. Jørgensen, F. C. Krebs, *Adv. Energy Mater.* **2011**, *1*, 68.
[33] T. T. Larsen-Olsen, B. Andreasen, T. R. Andersen, A. P. L. Böttiger, E. Bundgaard, K. Norrman, J. W. Andreasen, M. Jørgensen, F. C. Krebs, *Sol. Energy Mater. Sol. Cells* **2012**, *97*, 22.
[34] W. L. Yu, H. Zhang, Z. X. Fan, J. H. Zhang, H. T. Wei, D. Zhou, B. Xu, F. H. Li, W. J. Tian, B. Yang, *Energy Environ. Sci.* **2011**, *4*, 2831.
[35] Z. L. Chen, H. Zhang, W. L. Yu, Z. B. Li, J. D. Hou, H. T. Wei, B. Yang, *Adv. Energy Mater.* **2012**, DOI: 10.1002/aenm.201200741.
[36] T. T. Xu, Q. Q. Qiao, *Energy Environ. Sci.* **2011**, *4*, 2700.
[37] K. F. Jeltsch, M. Schädel, J. Bonekamp, P. Niyamakom, F. Rauscher, H. W. A. Lademann, I. Dumsch, S. Allard, U. Scherf, K. Meerholz, *Adv. Funct. Mater.* **2012**, *22*, 397.
[38] G. L. Grancini, R. S. S. Kumar, A. Abrusci, H. Yip, C. Li, A. Y. Jen, G. Lanzani, H. J. Snaith, *Adv. Funct. Mater.* **2012**, *22*, 2160.
[39] S. Dowland, T. Lutz, A. Ward, S. P. King, A. Sudlow, M. S. Hill, K. C. Molloy, S. A. Haque, *Adv. Mater.* **2011**, *23*, 2739.
[40] H. Chen, C. Lai, I. Wu, H. Pan, I. P. Chen, Y. Peng, C. Liu, C. Chen, P. Chou, *Adv. Mater.* **2011**, *23*, 5451.
[41] S. Q. Ren, L. Chang, S. Lim, J. Zhao, M. Smith, N. Zhao, V. Bulović, M. Bawendi, S. Gradečak, *Nano Lett.* **2011**, *11*, 3998.
[42] D. Celik, M. Krueger, C. Veit, H. F. Schleiermacher, B. Zimmermann, S. Allard, I. Dumsch, U. Scherf, F. Rauscher, P. Niyamakom, *Sol. Energy Mater. Sol. Cells* **2012**, *98*, 433.
[43] B. P. Khanal, E. R. Zubarev, *Angew. Chem. Int. Ed.* **2009**, *48*, 6888.
[44] E. D. Sone, E. R. Zubarev, S. I. Stupp, *Small* **2005**, *1*, 694.
[45] J. Y. Kim, K. Lee, N. E. Coates, D. Moses, T. Nguyen, M. Dante, A. J. Heeger, *Science* **2007**, *317*, 222.
[46] J. Y. Kim, S. H. Kim, H. Lee, K. Lee, W. L. Ma, X. Gong, A. J. Heeger, *Adv. Mater.* **2006**, *18*, 572.
[47] J. M. Griffing, L. Frank, Salisbury, *J. Am. Chem. Soc.* **1948**, *70*, 3416.